

## Validation of a multi-frequency electrical impedance tomography (mfEIT) system KHU Mark1: impedance spectroscopy and time-difference imaging

Tong In Oh<sup>1</sup>, Hwan Koo<sup>2</sup>, Kyung Heon Lee<sup>2</sup>, Sang Min Kim<sup>2</sup>,  
Jeehyun Lee<sup>3</sup>, Sung Wan Kim<sup>3</sup>, Jin Keun Seo<sup>3</sup> and Eung Je Woo<sup>2</sup>

<sup>1</sup> Department of Medical Physics and Bioengineering, University College London, UK

<sup>2</sup> College of Electronics and Information, Kyung Hee University, Korea

<sup>3</sup> Department of Mathematics, Yonsei University, Korea

E-mail: [ejwoo@khu.ac.kr](mailto:ejwoo@khu.ac.kr)

Received 24 July 2007, accepted for publication 7 January 2008

Published 11 February 2008

Online at [stacks.iop.org/PM/29/295](http://stacks.iop.org/PM/29/295)

### Abstract

Validation and interpretation of reconstructed images using a multi-frequency electrical impedance tomography (mfEIT) requires a conductivity phantom including imaging objects with known complex conductivity ( $\sigma + i\omega\epsilon$ ) spectra. We describe imaging experiments using the recently developed mfEIT system called the KHU Mark1 with the frequency range of 10 Hz to 500 kHz. Using a bio-impedance spectroscopy (BIS) system, we first measured complex conductivity spectra of different imaging objects including saline, agar, polyacrylamide, TX151, animal hide gelatin, banana and cucumber. Based on an analysis of how conductivity and permittivity affect measured complex boundary voltages, we suggested a new complex version of a multi-frequency time-difference image reconstruction algorithm. Imaging experiments were conducted to produce time-difference images of the objects at multiple frequencies using the proposed algorithm. Images of a conductor (stainless steel) and an insulator (acrylic plastic) were used to set a common scale bar to display all images. Comparing reconstructed time-difference images at multiple frequencies with measured complex conductivity spectra, we found that they showed an overall similarity in terms of changes in complex conductivity values with respect to frequency. However, primarily due to the limitation of the difference imaging algorithm, we suggest that multi-frequency time-difference images must be interpreted in terms of relative contrast changes with respect to frequency. We propose further imaging studies using biological tissues of known complex conductivity spectra and using human subjects to find clinical applications of the mfEIT system.

**Keywords:** multi-frequency EIT, complex conductivity, time-difference imaging

(Some figures in this article are in colour only in the electronic version)

## 1. Introduction

An electrical impedance tomography (EIT) system is called a multi-frequency EIT (mfEIT) system if it can inject currents into an imaging object and measure boundary voltages at multiple sinusoidal frequencies. Such a system is usually capable of producing images of a complex conductivity distribution inside the imaging object at multiple frequencies (Holder 2005). In this paper, we denote the complex conductivity as  $\sigma + i\omega\varepsilon$  where  $\sigma$  is the conductivity,  $\varepsilon$  is the permittivity and  $\omega$  is the angular frequency. Complex conductivity spectra of numerous biological tissues show frequency-dependent changes of conductivity and permittivity values (Geddes and Baker 1967, Gabriel *et al* 1996, Grimnes and Martinsen 2000). The mfEIT is used to provide spectroscopic information of those complex conductivity values. Examples of the mfEIT system include the Sheffield Mk 3.5 (Wilson *et al* 2001), UCLH Mk1b (Yerworth *et al* 2002), UCLH Mk2 (Yerworth *et al* 2003), Dartmouth system (Halter *et al* 2004), OXBACT III (Zhu *et al* 1994), ACT4 (Ross 2003) and KHU Mark1 (Oh *et al* 2007a, 2007b).

The goal of this paper is to evaluate the imaging performance of the recently developed KHU Mark1 mfEIT system (Oh *et al* 2007a, 2007b) through time-difference imaging experiments at multiple frequencies within the range of 10 Hz to 500 kHz. In order to validate and evaluate its performance, we should conduct imaging experiments using various objects with known complex conductivity spectra. The first part of the paper, therefore, deals with preparation of imaging objects and measurements of their complex conductivity spectra using a bio-impedance spectroscopy (BIS) system. We chose different materials of saline, stainless steel, acrylic plastic, agar, polyacrylamide, animal hide gelatine, TX151, cucumber and banana. After reviewing recipes to fabricate imaging objects using these materials, we will describe a method to obtain their complex conductivity spectra using the BIS system in the frequency range of 10 Hz to 500 kHz.

In the second part of the paper, we will describe imaging experiments of those objects with measured complex conductivity spectra. We will define a multi-frequency time-difference image reconstruction problem to produce images of  $\delta(\sigma + i\omega\varepsilon)$ , that is any change in  $\sigma + i\omega\varepsilon$  between time  $t_1$  and  $t_2$ , at multiple frequencies. We will explain why we should use complex voltages including both in-phase and quadrature components to reconstruct a time-difference complex conductivity image  $\delta(\sigma + i\omega\varepsilon)$  rather than separately using in-phase and quadrature components to produce images of  $\delta\sigma$  and  $\delta(\omega\varepsilon)$ , respectively. We will propose a complex version of a difference image reconstruction algorithm based on a complex sensitivity matrix. Reconstructed time-difference images at multiple frequencies will be compared with measured complex conductivity spectra for the validation of our mfEIT system.

## 2. Methods

### 2.1. Fabrication of imaging objects

To calibrate an mfEIT system, Holder *et al* (1996) have assessed three groups of materials in the frequency range of 10 kHz to 1 MHz and suggested two of them including the cucumber and a polyurethane sponge immersed in packed red cells. In this paper, in the frequency range of 10 Hz to 500 kHz, we tested nine different materials including saline, acrylic plastic, stainless steel, agar, polyacrylamide, animal hide gelatin, TX151, cucumber and banana. In this section, we first describe how to fabricate imaging objects of saline, agar, polyacrylamide, animal hide gelatin and TX151 with controlled conductivity values up to  $2 \text{ S m}^{-1}$  in each case obtained by adjusting the amount of NaCl.

**Table 1.** Composition of polyacrylamide (PAA) gel (Holder and Khan 1994).

Material	Amount	Role
Distilled water	100 ml	Principal ingredient
Sodium 4-styrene-sulfonate	2 g	Conductivity control
NaCl	$x$ g	Conductivity control
ACRYL/BIS 40% solution	100 ml	Solidification
10% ammonium persulfate solution	0.3 ml	Initiator
TEMED (tetramethylethylenediamine)	0.2 ml	Catalyst

**2.1.1. Saline.** Saline with a certain concentration of NaCl has been the most frequently used background medium of a conductivity phantom. Adding 9 g of NaCl into one liter of pure deionized water, we may get saline of  $1.94 \text{ S m}^{-1}$  conductivity and the relationship between the amount of NaCl and the conductivity is approximately linear for a conductivity value below  $2 \text{ S m}^{-1}$  (Grimnes and Martinsen 2000). Using double distilled water in our laboratory, we could obtain saline with conductivity  $\sigma = 0.23x + 0.05 \text{ S m}^{-1}$  for  $x \geq 1$  where  $x$  is the amount of NaCl in  $\text{g l}^{-1}$ . For  $x < 1 \text{ g l}^{-1}$ , we found that  $\sigma = 0.26x \text{ S m}^{-1}$ .

**2.1.2. Agar gel.** Agar gels have been widely used as imaging objects in EIT even though their conductivity values change with time when immersed in saline with a different conductivity value. Boiling distilled water mixed with  $15 \text{ g l}^{-1}$  agar (Yakuri Pure Chemicals Co., Japan) and  $x \text{ g l}^{-1}$  NaCl, we got an agar gel with a conductivity of  $\sigma = 0.22x + 0.18 \text{ S m}^{-1}$  for  $x \geq 1$  after cooling. For  $x < 1$ , we found that  $\sigma = 0.27x + 0.10 \text{ S m}^{-1}$ . Agar gels are quite soft and become dry when they are placed in the air.

**2.1.3. Polyacrylamide (PAA) gel.** PAA gels have been used in EIT experiments since they can be more stable over time when placed inside a saline tank (Holder and Khan 1994). As shown in table 1, we put 100 ml distilled water, 2 g sodium 4-styrene-sulfonate and  $x$  g of NaCl in a beaker. After mixing and boiling them together, we add 100 ml 40% ACRYL/BIS solution and stir well. Then, we add 0.3 ml 10% ammonium persulfate solution and 0.2 ml TEMED and stir well. The solution is poured into a mold with a desired shape and then the object is fixed in a few minutes. Though the conductivity of a PAA gel can be controlled by both sodium 4-styrene-sulfonate and NaCl, we fixed the amount of sodium 4-styrene-sulfonate and changed the amount of NaCl only. Following the recipe in table 1, the conductivity is given by  $\sigma = 0.89x^2 + 0.15x + 0.72 \text{ S m}^{-1}$  where  $x$  is the amount of NaCl in g in the final volume of 200 ml. PAA gels are rigid and quite brittle.

**2.1.4. Animal hide gelatin (AHG) gel.** AHG gels have been mostly used in MRI phantoms (Blechinger *et al* 1988). We found that they are also useful as a conductivity contrast material. Table 2 shows the composition of the gel. We need to prepare two bins with the mixture of ingredients in table 2. Heating must be done to  $90^\circ\text{C}$ . Combining 600 ml of bin 1 and 400 ml of bin 2, we add  $x$  g NaCl to the resulting 1 l volume of the mixture. Then, the conductivity is given as  $\sigma = 0.034x + 0.111 \text{ S m}^{-1}$  for  $x \geq 5 \text{ g}$ . For  $x < 5 \text{ g}$ ,  $\sigma = 0.037x + 0.006 \text{ S m}^{-1}$ . In MRI experiments, three different solidification ingredients are used to set imaging parameters of  $T1$  and  $T2$ . AHG gels are relatively soft and also rigid. However, since they are slowly dissolved when immersed in saline, it would be better to use them as a background material of a solid phantom without using saline.

**Table 2.** Composition of animal hide gelatin (AHG) gel (Blechinger *et al* 1988).

Material	Amount in bin 1	Amount in bin 2	Role
Distilled water	432 ml	308.5 ml	Principal ingredient
<i>n</i> -propanol	58 ml	41.5 ml	Antibacterial ingredient
<i>p</i> -methyl-benzoic acid	None	0.75 g	Antibacterial ingredient
40% formaldehyde	4 g	4 g	Antibacterial ingredient
Glycerol	210 ml	150 ml	Solidification
Animal hide gelatine	None	116 g	Solidification
Agar	31.5 g	None	Solidification
NaCl	$x$ g in 1 l	(After mixing)	Conductivity control

**Table 3.** Composition of TX151 gel (Mazzara *et al* 1996).

Material	Amount	Role
Distilled water	1 l	Principal ingredient
Agar	31 g	Solidification
TX151	16.9 g	Thickener
Sucrose	162.4 g	Permittivity control
NaCl	$x$ g	Conductivity control

**2.1.5. TX151 gel.** Searching for a better material to make conductivity phantoms, we found that a polysaccharide material, TX151 (Oil Center Research International, Lafayette, LA, USA), produces satisfactory results. Table 3 shows the composition of TX151 gels (Mazzara *et al* 1996). Adding NaCl and agar into distilled water, we stir the solution. After boiling it, we add TX151 and sucrose. Stirring the mixed solution well, we filter it using a fine metallic net. The filtered solution must be quickly poured into a mold since it sets relatively fast. The conductivity is given by  $\sigma = 0.14x + 0.26 \text{ S m}^{-1}$  for  $x \geq 10$  g where  $x$  is the amount of NaCl in the final volume of 1 l. For  $x < 10$  g,  $\sigma = 0.15x + 0.11 \text{ S m}^{-1}$ . We found that controlling permittivity by adjusting the amount of sucrose is difficult below 500 kHz. TX151 gels are quite rigid but soft enough to be cut easily. Unlike AHG gels, they are relatively stable in saline.

## 2.2. Measurement of the complex conductivity spectrum using BIS

**2.2.1. The BIS and sample chamber.** For the measurement of complex conductivity spectrum, we used the BIS system shown in figure 1(a) that is basically a one-channel mFEIT system developed by Oh *et al* (2007a, 2007b). Within the frequency range of 10 Hz to 500 kHz, we chose ten frequencies of 10, 50, 100, 1000, 5000, 10 000, 50 000, 100 000, 250 000, and 500 000 Hz for impedance measurements. In order to use the four-electrode method, we constructed a sample chamber (figure 1(b)) with separate pairs of current injection and voltage measuring electrodes (figure 1(c)). All electrodes were made of stainless steel and the size of the current injection electrodes was  $100 \times 100 \text{ mm}^2$ . The disk-shaped voltage measuring electrodes at the center of the chamber had a diameter of 8 mm.

**2.2.2. The parallel RC model.** We modeled the impedance of a sample as a parallel RC circuit. Then, the impedance can be represented as

$$\mathbf{Z} = \frac{R}{1 + \omega^2 R^2 C^2} - \mathrm{j} \frac{\omega R^2 C}{1 + \omega^2 R^2 C^2} = R_M + \mathrm{j} X_M \quad (1)$$

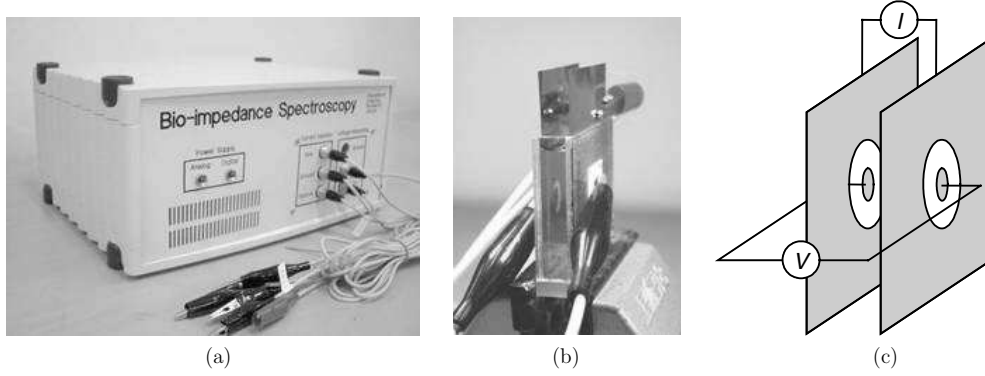


**Figure 1.** (a) BIS, (b) sample chamber and (c) electrode configuration.

where  $R_M$  and  $X_M$  are measured resistance and reactance of  $\mathbf{Z}$  using the BIS system, respectively. Assuming that the sample is homogeneous and isotropic, we have

$$R = \frac{1}{\sigma} \frac{l}{S} \quad \text{and} \quad C = \alpha \varepsilon \frac{S}{l} \quad (2)$$

where  $l$  and  $S$  are the length and cross-sectional area of the sample chamber, respectively. Here, we approximated the effect of the finite geometry of the sample chamber by using the scale factor  $\alpha$  in the formula for  $C$ . Then, we get

$$\sigma = \frac{R_M}{R_M^2 + X_M^2} \frac{l}{S} \quad \text{and} \quad \alpha \varepsilon = -\frac{1}{\omega} \frac{X_M}{R_M^2 + X_M^2} \frac{l}{S}. \quad (3)$$

In order to remove the scale factor  $\alpha$ , we first measured the impedance of the sample chamber filled with air using the two-electrode method connecting each pair of current and voltage electrodes together. To make the measured data fit in the measurement range of the BIS system, we added a  $120 \, \Omega$  metal film resistor in parallel with the chamber. This gave us the value of  $\alpha \varepsilon_0$  using the chamber. In subsequent impedance measurements using different samples, we computed a relative permittivity  $\varepsilon_R$  as  $\varepsilon_R = \frac{\alpha \varepsilon}{\alpha \varepsilon_0}$ . Then, we set the permittivity of the sample as  $\varepsilon = \varepsilon_R \times 8.854 \times 10^{-12} \, \text{F m}^{-1}$ .

### 2.3. Multi-frequency time-difference image reconstruction

**2.3.1. Problem definition.** Let an imaging object occupy a two- or three-dimensional region  $D$  with its boundary  $\partial D$ . Surface electrodes  $\mathcal{E}_j$  for  $j = 1, \dots, n$  are attached to  $\partial D$ . When we inject sinusoidal current  $i(t) = I \sin(\omega t)$  in amperes through a pair of surface electrodes, it induces a distribution of voltage  $v(\mathbf{r}, t) = V(\mathbf{r}) \sin(\omega t + \theta(\mathbf{r}))$  in volts at a position  $\mathbf{r}$  throughout the domain  $D$ . Using the phasor notation, the complex voltage  $u_\omega$  at  $\mathbf{r} = (x, y, z)$  can be expressed as  $u_\omega(\mathbf{r}) = v_\omega(\mathbf{r}) + i h_\omega(\mathbf{r}) = V(\mathbf{r}) \angle \theta(\mathbf{r}) = V(\mathbf{r}) \cos \theta(\mathbf{r}) + i V(\mathbf{r}) \sin \theta(\mathbf{r})$ . In an mfEIT system, we may measure the complex voltage  $u_\omega$  between pairs of surface electrodes at multiple frequencies. When the frequency is relatively low, it satisfies the following elliptic partial differential equation (Holder 2005):

$$\begin{cases} \nabla \cdot ((\sigma(\mathbf{r}, \omega) + i\omega\varepsilon(\mathbf{r}, \omega)) \nabla u_\omega) = 0 & \text{in } D \\ -(\sigma(\mathbf{r}, \omega) + i\omega\varepsilon(\mathbf{r}, \omega)) \nabla u_\omega \cdot \mathbf{n} = g & \text{on } \partial D \end{cases} \quad (4)$$

where both  $\sigma$  and  $\varepsilon$  depend on the position  $\mathbf{r}$  and the angular frequency  $\omega$ . Here,  $\mathbf{n}$  is the outward unit normal vector on  $\partial D$  and  $g$  is the magnitude of the current density on  $\partial D$  due to

the injection current. Setting a reference voltage having  $\int_{\partial D} u_\omega = 0$ , we can obtain a unique solution  $u_\omega$  of (4) from a given complex conductivity distribution  $\gamma = \sigma + i\omega\varepsilon$  in  $D$  and  $g$  on  $\partial D$ . The boundary value problem in (4) can also be expressed as the following coupled system:

$$\begin{cases} \nabla \cdot (\sigma \nabla v_\omega) - \nabla \cdot (\omega \varepsilon \nabla h_\omega) = 0 & \text{in } D \\ \nabla \cdot (\omega \varepsilon \nabla v_\omega) + \nabla \cdot (\sigma \nabla h_\omega) = 0 & \text{in } D \\ \mathbf{n} \cdot (-\sigma \nabla v_\omega + \omega \varepsilon \nabla h_\omega) = g & \text{on } \partial D \\ \mathbf{n} \cdot (-\sigma \nabla h_\omega - \omega \varepsilon \nabla v_\omega) = 0 & \text{on } \partial D. \end{cases} \quad (5)$$

**2.3.2. Complex version of difference image reconstruction algorithm.** We note that both  $\sigma$  and  $\varepsilon$  affect  $v_\omega$  and  $h_\omega$  as shown in (5). This has been observed by Scalfe *et al* (1994) and they suggested a time-difference imaging method considering this coupling for an induced-current EIT system. For the injection-current mEIT system being described in this paper, we also should not separately use  $v_\omega$  and  $h_\omega$  to produce images of  $\delta\sigma$  and  $\delta(\omega\varepsilon)$ , respectively.

In this paper, we consider only the multi-frequency time-difference imaging between times  $t_1$  and  $t_2$ . We suggest a complex version of a time-difference image reconstruction algorithm based on the following linear approximation (Cheney *et al* 1990, Mueller *et al* 1999, Lionheart *et al* 2005):

$$\nabla \cdot (\gamma_\omega \nabla \delta u_\omega^j) \approx \nabla \cdot (\delta \gamma_\omega \nabla u_{\omega, t_1}^j)$$

where  $u_{\omega, t}^j$  is the voltage  $u_\omega^j$  at time  $t$ ,  $\delta u_\omega^j = u_{\omega, t_2}^j - u_{\omega, t_1}^j$  and

$$\begin{aligned} \delta \gamma_\omega(\mathbf{r}) &= \delta \sigma_\omega(\mathbf{r}) + i \delta \omega \varepsilon_\omega(\mathbf{r}) \\ &= \sigma(\mathbf{r}, \omega, t_2) - \sigma(\mathbf{r}, \omega, t_1) + i\omega(\varepsilon(\mathbf{r}, \omega, t_2) - \varepsilon(\mathbf{r}, \omega, t_1)). \end{aligned}$$

In mEIT, we try to reconstruct time-difference images of  $\delta \gamma_\omega$  at various frequencies using the following misfit functional:

$$\Psi(\delta \gamma_\omega) = \sum_{j=1}^N \left\| \delta u_\omega^j|_{\partial \Omega} - (f_{\omega, t_2}^j - f_{\omega, t_1}^j) \right\|^2 \quad (6)$$

where  $\|\cdot\|$  denotes the complex  $L^2$ -norm on the boundary  $\partial D$ ,  $\delta u_\omega^j$  is the time-difference complex voltage corresponding to the predicted time-difference complex conductivity  $\delta \gamma_\omega$  and  $f_{\omega, t}^j$  is the measured complex boundary voltage at time  $t$  corresponding to the  $j$ th injection current. Using the approximation  $\int_D \delta \gamma_\omega \nabla u_\omega^j \cdot \nabla u_\omega^k \, d\mathbf{r} \approx \int_{\partial D} \delta u_\omega^j g_k \, ds$ , the least-squares misfit method of (6) leads to the following approximation for  $\delta \gamma_\omega$ :

$$\int_D \delta \gamma_\omega \nabla u_\omega^j \cdot \nabla u_\omega^k \, d\mathbf{r} = \int_{\partial D} (f_{\omega, t_2}^j - f_{\omega, t_1}^j) g_k \, ds, \quad j, k = 1, \dots, n-1. \quad (7)$$

The time-difference image reconstruction algorithm for  $\delta \gamma_\omega$  is based on the discretized version of (7) and the truncated singular value decomposition. The major difference from previous methods is that we process complex voltages  $f_{\omega, t}^j$  using a complex sensitivity matrix that depends on the frequency  $\omega$ . We reconstruct an image of  $\delta \gamma_\omega$  at each chosen frequency  $\omega$  within the range of 10 Hz to 500 kHz and separately display  $\delta \sigma_\omega$  and  $\delta(\omega \varepsilon_\omega)$ .

#### 2.4. Imaging experiments

We constructed a two-dimensional saline phantom with  $0.137 \, \text{S m}^{-1}$  conductivity. The phantom with 200 mm diameter and 100 mm height was equipped with 16 equally spaced

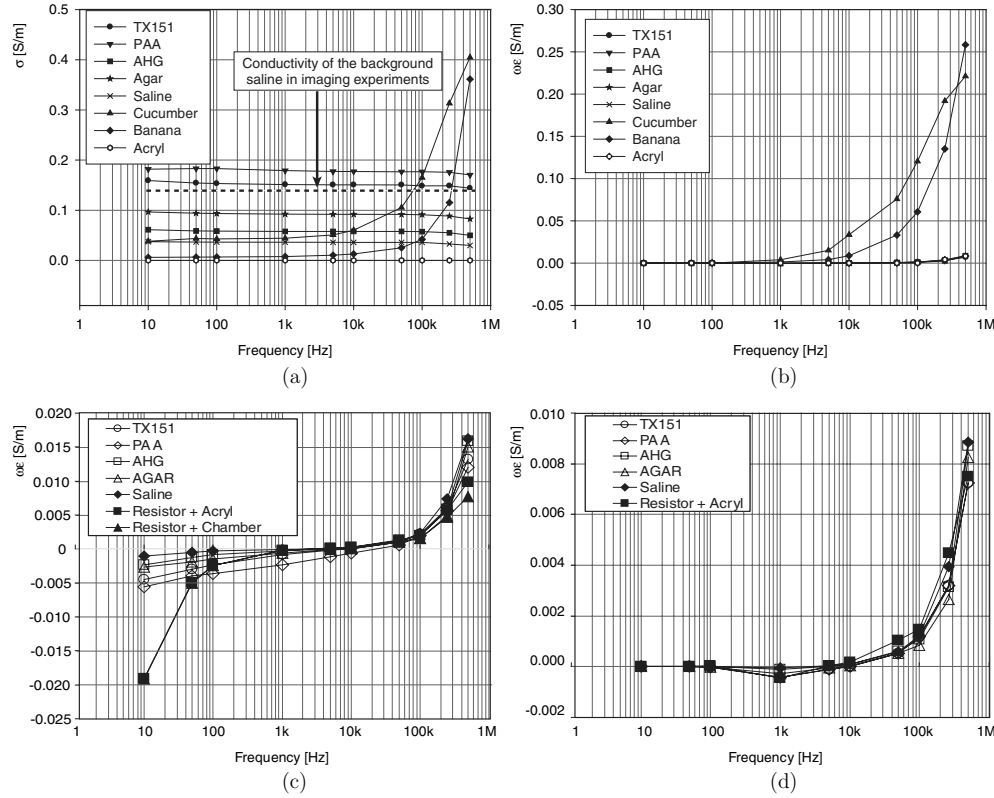


**Figure 2.** (a)  $\sigma$  and (b)  $\omega\epsilon$  spectra. Magnified  $\omega\epsilon$  spectra of non-biological materials only: (c) before and (d) after compensating the scale factor  $\alpha$  in (3). These data were measured by using the BIS system in figure 1. In (c) and (d), negative values at low frequencies stemmed from phase errors of the BIS system in measuring very small reactance values.

stainless steel electrodes. In each experiment, we prepared imaging objects as described in section 2.1. As soon as we finished measurements of complex conductivity spectra, we placed the objects inside the phantom. Collecting complex boundary voltage data using a 16-channel KHU Mark1 mFEIT system (Oh *et al* 2007a, 2007b), we reconstructed time-difference images of the phantom using the algorithm described in section 2.3.2. As the reference voltage data  $f_{\omega, t_1}^j$  in (7), we used the data from the homogeneous saline phantom. The voltage data  $f_{\omega, t_2}^j$  in (7) were obtained after placing imaging objects inside the phantom.

### 3. Results

Figures 2(a) and (b) show measured  $\sigma$  and  $\omega\epsilon$  spectra of eight different materials, respectively, at 25 °C. As described in section 2.1, the conductivities of non-biological materials including saline, agar, PAA, AHG and TX151 gels can be adjusted by changing the amount of NaCl. In figure 2(a), however, we fixed the amount to show only the frequency-dependent changes of their conductivities. Since there exist significant differences in  $\omega\epsilon$  spectra between biological and non-biological materials, we plotted  $\omega\epsilon$  spectra of non-biological materials only in figures 2(c) and (d) using a magnified scale. In (c), we plotted  $\omega\epsilon$  spectra before compensating



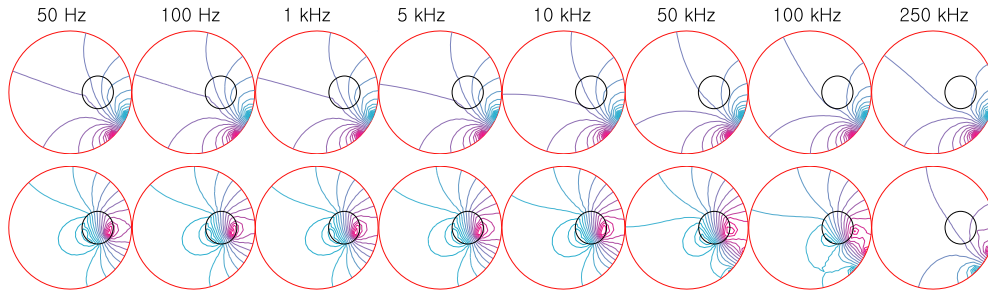


**Figure 3.** Numerical example showing equipotential lines of the real (top) and imaginary (bottom) parts of the complex potential  $u_\omega = v_\omega + ih_\omega$  at different frequencies.

the scale factor  $\alpha$  in (3) and included the  $\omega\varepsilon$  spectrum of the sample chamber itself with the  $120\ \Omega$  resistor in parallel. The plots in (d) were obtained after compensating the scale factor  $\alpha$  by using the  $\omega\varepsilon$  spectrum of the sample chamber in (c). In (c) and (d), negative  $\omega\varepsilon$  values at low frequencies stemmed from phase errors of the BIS system in measuring very small reactance values at those frequencies.

We have developed a forward solver to get a numerical solution of the complex voltage  $u_\omega$  in (4) using the finite-element method. Figure 3 shows equipotential lines of the complex voltage  $u_\omega = v_\omega + ih_\omega$  at chosen frequencies between 10 Hz and 500 kHz. In this numerical example, current was injected between a pair of neighboring electrodes. The background conductivity was  $0.137\ \text{S m}^{-1}$  and the complex conductivity of the circular anomaly was chosen as the measured value of the banana illustrated in figure 2. The time-difference image reconstruction algorithm in (7) was validated by performing numerical simulations using the forward solver.

Figures 4(a)–(c) show time-difference images of non-biological objects including the acrylic plastic, stainless steel and TX151, respectively, inside the phantom at chosen frequencies of 50, 100, 1000, 5000, 10 000, 50 000, 100 000 and 250 000 Hz. All images were drawn to have the same absolute scale that was determined from difference images of the insulator and conductor. For acrylic plastic and TX151 objects,  $\delta\sigma$  images do not show any change of conductivity with frequency and  $\delta(\omega\varepsilon)$  images indicate that permittivity effects are negligible. Images of agar, PAA and AHG gels were very similar to those of the TX151 object. Images of the stainless steel object need a careful interpretation. At low frequencies of 50 and 100 Hz, the stainless steel clearly appears in  $\delta(\omega\varepsilon)$  images whereas it is dimmed in  $\delta\sigma$  images. This can be explained as the effects of the metal–electrolyte interface phenomena producing a charge double layer at the interface and resulting in distributed capacitors around the metal.

Figures 5(a) and (b) show time-difference images of biological objects, the banana and cucumber, respectively. As expected from measured spectra of  $\sigma$  and  $\omega\varepsilon$  in figure 2, these images clearly show changes of both  $\sigma$  and  $\omega\varepsilon$  with respect to frequency. Comparing  $\delta\sigma$  and  $\delta(\omega\varepsilon)$  images of the banana and cucumber, we can observe that  $\sigma$  and  $\omega\varepsilon$  of the cucumber start to increase from its low-frequency values earlier than those of the banana as illustrated in figure 2. Figure 6 shows images of non-biological and biological objects together.

#### 4. Discussion and conclusion

Performance of an mFEIT system must be evaluated in terms of its ability to produce spectroscopic images of a complex conductivity distribution. This can be done by conducting



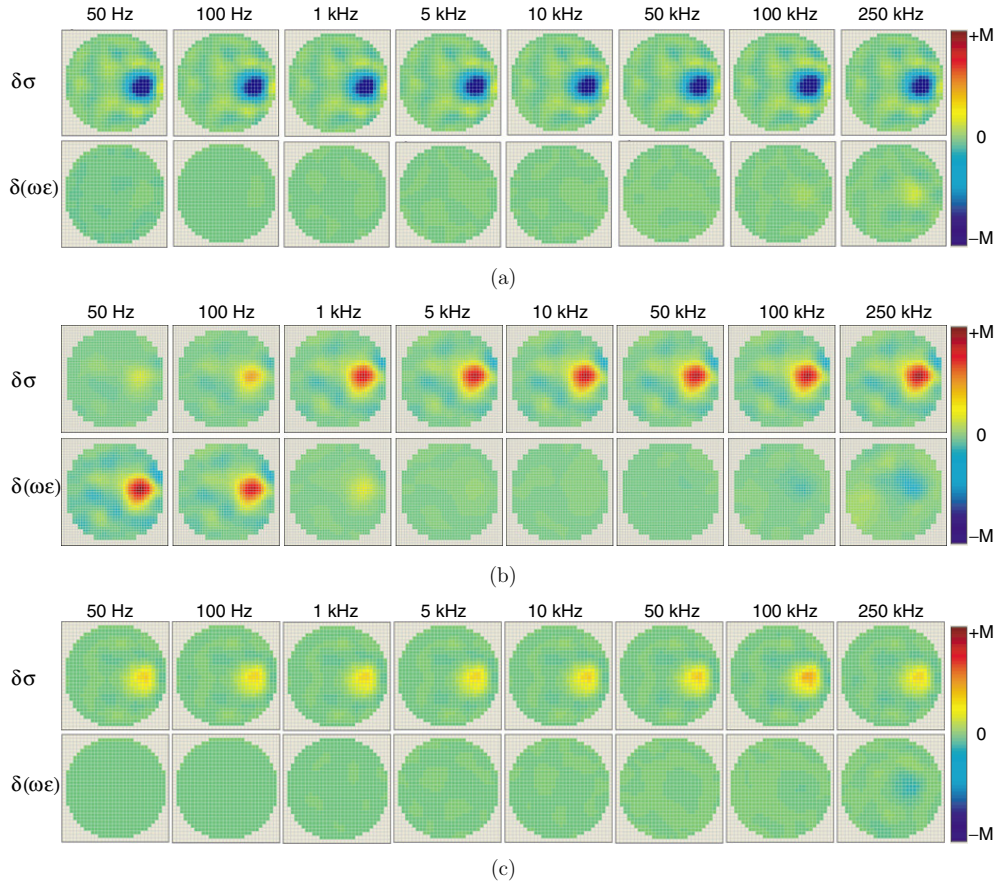


**Figure 4.** Time-difference images of a non-biological object using the reference data from the homogeneous saline phantom: (a) acrylic plastic, (b) stainless steel and (c) TX151.

imaging experiments using objects with known complex conductivity spectra. We have, therefore, measured complex conductivity spectra of different non-biological and biological materials using a BIS system. Conductivities of the banana and cucumber increased significantly above around 10 kHz (figure 2(a)). Conductivities of non-biological materials show a negligible change with frequency up to 500 kHz. The difference between biological and non-biological materials was more significant in  $\omega\epsilon$  spectra (figure 2(b)). At frequencies greater than 10 kHz,  $\omega\epsilon$  values of the banana and cucumber were comparable to their  $\sigma$  values, suggesting that we should not ignore the permittivity term in (4) beyond 10 kHz.

Before experiments, we calibrated the BIS system as well as the mfEIT system by using the method described in Oh *et al* (2007b). The most difficult part of the calibration procedure was to obtain the orthogonality between in-phase and quadrature parts of measured voltage data. Stray capacitances existed in printed circuit board patterns, switches, connectors and cables. Furthermore, tolerances and non-ideal frequency characteristics of electronic components, analog band-limiting filters and clock delays in digital phase-sensitive demodulations produced systematic phase shifts. When we performed a system calibration using a resistor, the resistor itself could have some reactance value at high frequencies. At low frequencies, reactance

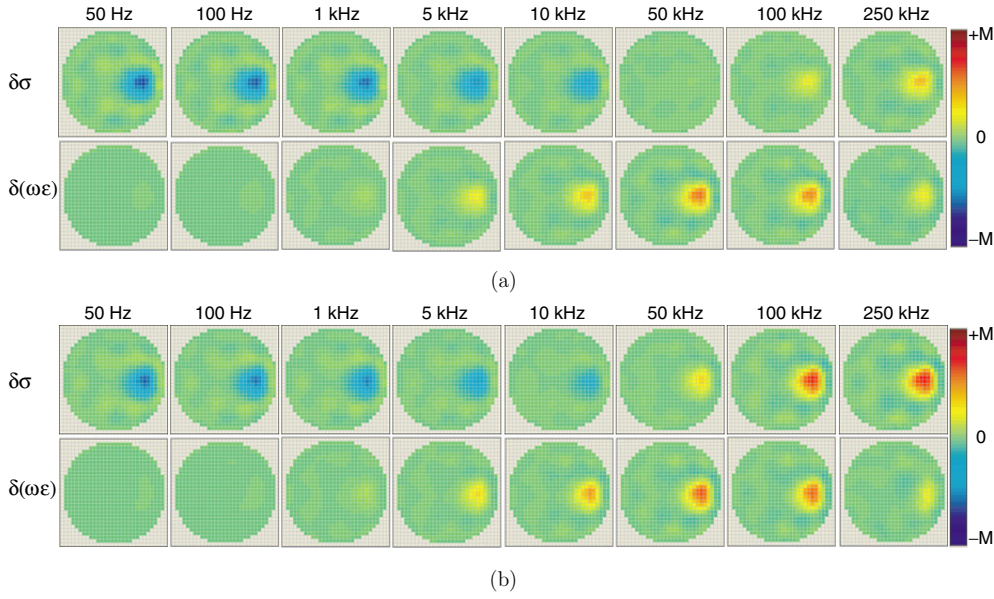


**Figure 5.** Time-difference images of a biological object using the reference data from the homogeneous saline phantom: (a) banana and (b) cucumber.

values were often too small to be measured with a good accuracy. Considering all these, we speculate that there existed some errors in measured complex conductivity values especially in  $\omega\epsilon$  spectra even after the system calibration. This suggests future work to improve the accuracy of the BIS system in measuring absolute complex conductivity values at a wider frequency range. However, we believe that the results in figure 2 showing significant differences among complex conductivity spectra of biological and non-biological materials are useful enough for the performance evaluation of the mFEIT system, which is the main goal of the paper.

Reconstructed time-difference images of non-biological and biological objects (figures 4, 5 and 6) were in general quite comparable to measured  $\sigma$  and  $\omega\epsilon$  spectra. Some caution was necessary when we interpreted images of a metallic object (stainless steel in this paper) in saline since the object appeared as a high-permittivity material at low frequencies. From repeated imaging experiments using the stainless steel object without and also with surface polishing, we could obtain very similar results. We believe that the permittivity effect at low frequencies is primarily due to distributed capacitors at the metal–electrolyte interface. We could observe a bigger permittivity effect by using a copper object.

Conductivities of the banana and cucumber at low frequencies were lower than the background conductivity of  $0.137 \text{ S m}^{-1}$  (see figure 2(a)) and they appear as low-conductivity regions (blue color) in figure 5. At high frequencies, they appear as high-conductivity regions since their conductivity values increase above the background conductivity. However, the intersecting frequencies where the objects disappear in time-difference images tend to be lower than the intersecting frequencies of around 250 and 70 kHz for the banana and cucumber, respectively, in measured spectra (see figure 2(a)). We speculate that this is primarily related with a limitation of the image reconstruction algorithm that produces time-difference not static images using the linearization method.

The  $\delta(\omega\epsilon)$  images of the banana and cucumber in figure 5 show a reduced contrast at 250 kHz, compared to 50 and 100 kHz. Since this is not expected from the plots in figure 2(b),

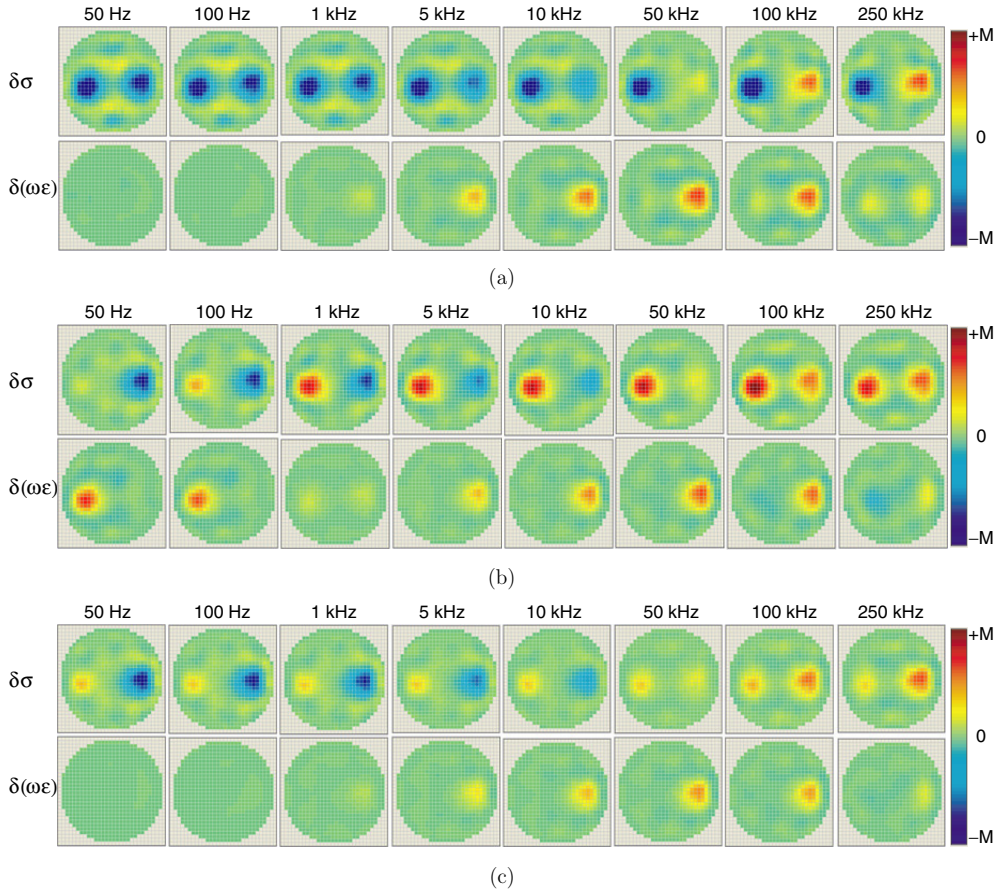


**Figure 6.** Time-difference images of non-biological and biological objects together using the reference data from the homogeneous saline phantom: (a) acrylic plastic/banana, (b) stainless steel/banana and (c) TX151/banana. The non-biological object and banana were placed on the left and right side, respectively.

we examined the measured time-difference voltage data  $f_{\omega,t_2} - f_{\omega,t_1}$  in (7) that were used to produce the  $\delta(\omega\epsilon)$  images. The imaginary parts of the voltage differences gradually increased from 50 Hz to 50 kHz and decreased after 50 kHz. At 250 kHz, the reduced imaginary parts of the voltage differences were similar to those at 5 kHz. This indicates that the reduced contrast at 250 kHz cannot be explained by the limitation of the linearized time-difference algorithm only. Here, we note that common systematic errors could have been cancelled out in the time-difference images whereas the measured complex conductivity spectra should have included those errors. This suggests that we need to more thoroughly investigate the accuracy of the BIS measurements at high frequencies in our future studies.

From figure 6, we can see that each time-difference image of two separated objects is almost an algebraic sum of two images of each object alone. However, it is not clear whether we can generalize this observation to a more complicated complex conductivity distribution. Due to the inherent nature of the difference image reconstruction method, the image contrast does not accurately reflect true differences in complex conductivity values. This can be seen



in figure 6 where either the insulator or conductor is imaged together with the banana object. Therefore, we suggest that multi-frequency time-difference images must be interpreted in terms of relative contrast changes with respect to frequency among pixels.

The primary goal of this paper was to find out the relation between complex conductivity spectra and reconstructed multi-frequency time-difference images using the complex version of the time-difference image reconstruction algorithm. Therefore, we performed only two-dimensional phantom experiments to avoid other technical issues related with three-dimensional imaging methods. In three-dimensional imaging experiments, we expect that reconstructed images will show some differences in terms of contrast changes with respect to frequency. However, we believe that the overall similarity between complex conductivity spectra and time-difference images will be preserved.

Complex conductivity values of saline, agar, PAA, AHG and TX151 change with time primarily due to evaporation. When they are placed together inside a phantom, their contrast gradually changes due to movements of ions across contact areas. For biological objects, similar phenomena occur and the variability among samples is bigger. Therefore, in this paper, we have not tried to store and reuse the imaging objects. If possible, fabrication of a standardized conductivity phantom with enough contrast and long-term stability will be very useful for comparative experimental studies.

Future studies are planned and in progress. Most of all, the method described in this paper should be tested in human subjects seeking for meaningful clinical applications. We believe that the validation study in this paper will provide a guideline to interpret images from human subjects. Effects of three-dimensional current flows inside the human body with an irregular boundary shape must be investigated in future studies of image reconstruction algorithms. Other algorithmic issues including different kinds of regularization and numerical implementation methods should be also considered. In addition to the time-difference imaging method, a frequency-difference imaging should be pursued since a time-reference data set is not available in some application areas.

## Acknowledgments

This work was supported by the SRC/ERC program of MOST/KOSEF (R11-2002-103) and the MOST/KICOS grant (M60501000035-05A0100-03510).

## References

- Blechinger J C, Madsen E L and Frank G R 1988 Tissue mimicking gelatin-agar gels for use in magnetic resonance imaging phantoms *Med. Phys.* **15** 629–36
- Cheney M, Isaacson D, Newell J C, Simske S and Goble J 1990 NOSER: an algorithm for solving the inverse conductivity problem *Int. J. Imaging Syst. Technol.* **2** 66–75
- Gabriel S, Lau R W and Gabriel C 1996 The dielectric properties of biological tissues: II. Measurements in the frequency range 10 Hz to 20 GHz *Phys. Med. Biol.* **41** 2251–69
- Geddes L A and Baker L E 1967 The specific resistance of biological material: a compendium of data for the biomedical engineer and physiologist *Med. Biol. Eng.* **5** 271–93
- Grimnes S and Martinsen O G 2000 *Bioimpedance and Bioelectricity Basics* (London, UK: Academic)
- Halter R, Hartov A and Paulsen K D 2004 Design and implementation of a high frequency electrical impedance tomography system *Physiol. Meas.* **25** 379–90
- Holder D 2005 *Electrical Impedance Tomography: Methods, History and Applications* (Bristol, UK: Institute of Physics Publishing)
- Holder D, Hanquan Y and Rao A 1996 Some practical biological phantoms for calibrating multifrequency electrical impedance tomography *Physiol. Meas.* **17** A167–77

- Holder D and Khan A 1994 Use of polyacrylamide gels in a saline-filled tank to determine the linearity of the Sheffield Mark 1 electrical impedance tomography (EIT) system in measuring impedance disturbances *Physiol. Meas.* **15** A45–50
- Lionheart W, Polydorides N and Borsic A 2005 The reconstruction problem *Electrical Impedance Tomography: Methods, History and Applications* ed D S Holder (Bristol, UK: Institute of Physics Publishing)
- Mazzara G P, Briggs R W, Wu Z and Steinbach B G 1996 Use of a modified polysaccharide gel in developing a realistic breast phantom for MRI *Mag. Res. Imaging* **14** 639–48
- Mueller J L, Isaacson D and Newell J C 1999 A reconstruction algorithm for electrical impedance tomography data collected on rectangular electrode arrays *IEEE Trans. Biomed. Eng.* **46** 1379–86
- Oh T I, Woo E J and Holder D 2007a Multi-frequency EIT system with radially symmetric architecture: KHU Mark I *Physiol. Meas.* **28** S183–196
- Oh T I, Lee K H, Kim S M, Koo H, Woo E J and Holder D 2007b Calibration methods for a multi-channel multi-frequency EIT system *Physiol. Meas.* **28** 1175–88
- Ross A S 2003 An adaptive current tomograph for breast cancer detection *PhD Thesis* Rensselaer Polytechnic Institute, Troy, NY, USA
- Scalfe J M, Tozer R C and Freeston I L 1994 Conductivity and permittivity images from an induced current electrical impedance tomography system *IEE Proc. Sci. Meas. Technol.* **141** 356–62
- Yerworth R J, Bayford R H, Brown B, Milnes P, Conway M and Holder D S 2003 Electrical impedance tomography spectroscopy (EITS) for human head imaging *Physiol. Meas.* **24** 477–89
- Yerworth R J, Bayford R H, Cusick G, Conway M and Holder D S 2002 Design and performance of the UCLH Mark 1b 64 channel electrical impedance tomography (EIT) system, optimized for imaging brain function *Physiol. Meas.* **23** 149–58
- Wilson A J, Milnes P, Waterworth A R, Smallwood R H and Brown B H 2001 Mk3.5: a modular, multi-frequency successor to the Mk3a EIS/EIT system *Physiol. Meas.* **22** 49–54
- Zhu Q S, McLeod C N, Denyer C W, Lidgley F J and Lionheart W R B 1994 Development of a real-time adaptive current tomography *Physiol. Meas.* **15** A37–43